

Dalton Transactions

An international journal of inorganic chemistry

Accepted Manuscript

This article can be cited before page numbers have been issued, to do this please use: B. Vlasisavljević and S. A. Fosu, *Dalton Trans.*, 2025, DOI: 10.1039/D5DT01898F.



This is an Accepted Manuscript, which has been through the Royal Society of Chemistry peer review process and has been accepted for publication.

Accepted Manuscripts are published online shortly after acceptance, before technical editing, formatting and proof reading. Using this free service, authors can make their results available to the community, in citable form, before we publish the edited article. We will replace this Accepted Manuscript with the edited and formatted Advance Article as soon as it is available.

You can find more information about Accepted Manuscripts in the [Information for Authors](#).

Please note that technical editing may introduce minor changes to the text and/or graphics, which may alter content. The journal's standard [Terms & Conditions](#) and the [Ethical guidelines](#) still apply. In no event shall the Royal Society of Chemistry be held responsible for any errors or omissions in this Accepted Manuscript or any consequences arising from the use of any information it contains.

Journal Name

ARTICLE TYPE

Cite this: DOI: 00.0000/xxxxxxxxxx

Stereoselective Ring Opening Polymerization of Lactide by Chiral Aluminum Salan Catalysts[†]Samuel A. Fosu^a and Bess Vlasisavljević^{a,b,*}Received Date
Accepted Date

DOI: 00.0000/xxxxxxxxxx

The stereocontrolled ring-opening polymerization of lactide via rational catalyst design remains a challenge due, in no small part, to the presence of the various stereoisomers of lactide and the resulting structural complexity that arises along the reaction profile. In practice, the stereochemistry leads to polylactides with different structures and properties, although the syndiotactic product is desired. Density functional theory (DFT) can contribute by identifying the underlying non-covalent interactions that favor one reaction profile over another. Herein, we investigate the initiation step of a chloride-substituted, bipyrrrolidine-based aluminum-alkoxy salan catalyst that has shown kinetic preference for the stereoselective ring-opening of *meso*-lactide at the carbonyl unit adjacent to the *R* stereocenter. Moreover, when experiments are performed under thermodynamic control, the initiation product in which the *S* stereocenter is ultimately adjacent to aluminum is favored. Following an exhaustive conformational search of both minima and transition state structures, DFT reaction mechanisms are consistent with these observations. Specifically, the rate-determining transition states corresponding to ring opening at the *R* stereocenter are stabilized by crucial ligand-chain non-covalent interactions including hydrogen bonding. In turn, the rate determining transition state for ring-opening at the *S*-stereocenter lies only 0.6 kcal/mol higher in energy, further emphasizing the importance in using conformational sampling in modeling such processes.

1 Introduction

Polylactide (PLA) has attracted great interest as a potential renewable substitute for petroleum-based plastics such as polyethylene, polyvinylchloride, and polystyrene.^{1–4} The high attractiveness of this aliphatic polyester is due to its biodegradability, bioprocessability, and wide availability from biobased sources such as corn starch, sugarcane, and wheat.^{5–7} PLAs are also desired due to their unique microstructures, which influence their physical properties such as melting point, rigidity, solubility, crystallinity, and glass transition temperature.^{8,9} The stereoselective ring-opening polymerization (ROP) of lactide (LA) is reported as an efficient technique to tune the structure and properties of PLA.^{8,10–12} ROP of LA allows for greater control of the molecular architecture of PLA compared to synthesis via polycondensation of LA.⁸ However, achieving stereocontrolled ROP through rational catalyst design remains a challenge due to the presence of different stereoisomers of LA, which could yield PLAs with different structures and properties.¹³

When stereocontrolled ROP is achieved, LA units are inserted

into the growing polymer chain in an orderly manner according to their stereochemistry (Figure 1).⁸ In chiral isotactic PLA, all stereocenters are oriented toward the same side of the chain, producing D-LA or L-LA. However, ROP of racemic mixtures of D-LA and L-LA may result in isotactic diblock or multiblock PLA, or heterotactic PLA. On the other hand, ROP of *meso*-LA yields heterotactic or syndiotactic PLA.^{2,13,14} Control of the polymerization of enantiopure or racemic mixtures of LA could lead to the ultimate control of its properties. To rationally design catalysts to achieve desirable PLAs, it is essential to understand the origin of stereocontrol in the ROP of LA. This could yield unique polymers for applications in drug delivery, tissue engineering, biomedical implants, and microelectronics.^{6,8,15}

For greater control of the polymer architecture, ROP via a coordination-insertion mechanism is recommended (Figure 2).¹⁶ In the classical case, the critical steps in the ROP mechanism involve coordination of the monomer to the metal (and insertion between the metal and alkoxy group) via **TS1**. The subsequent ring-opening step via **TS2** involves cleavage of a C–O bond adjacent to the opposite stereogenic center.¹⁷ However, additional intermediate steps critical to stereoselectivity in the ROP of LA by the prototype Spassky's catalyst have been proposed in recent studies.^{13,17–21} These include a potential chain-monomer exchange after **TS1**, as well as possible catalyst re-organization leading to changes in the ligand wrapping around the metal (Fig-

Address: ^aUniversity of South Dakota, Department of Chemistry, 414 E Clark Street, Vermillion, SD, 57069, USA. ^bUniversity of Iowa, Department of Chemistry, 230 N. Madison Street, Iowa City, IA, 52242 USA E-mail: bess-vlasisavljevic@uiowa.edu

[†] Electronic Supplementary Information (ESI) available: [details of any supplementary information available should be included here]. See DOI: 00.0000/00000000.



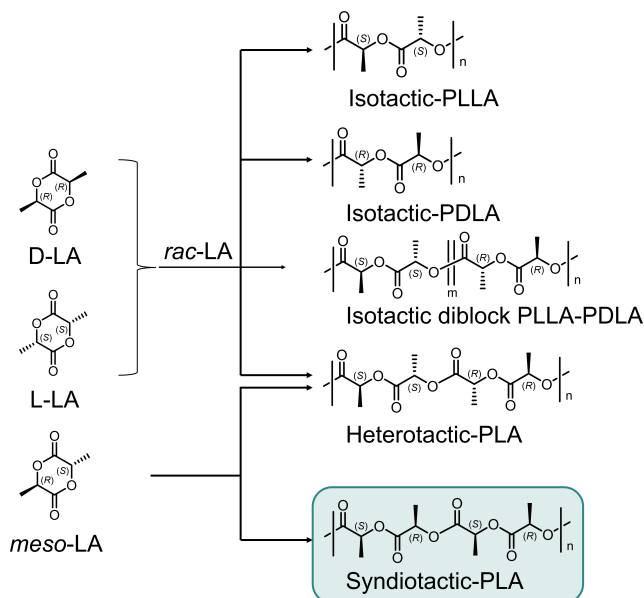


Fig. 1 Microstructures of polylactide (PLA) obtained via the stereoselective ring-opening polymerization (ROP) of lactide (LA). The stereoisomers of LA (e.g., D-LA, L-LA, or *meso*-LA) are shown along with the possible isotactic, heterotactic, or syndiotactic products. The desired product is syndiotactic PLA, highlighted in the teal box.

ure 2).

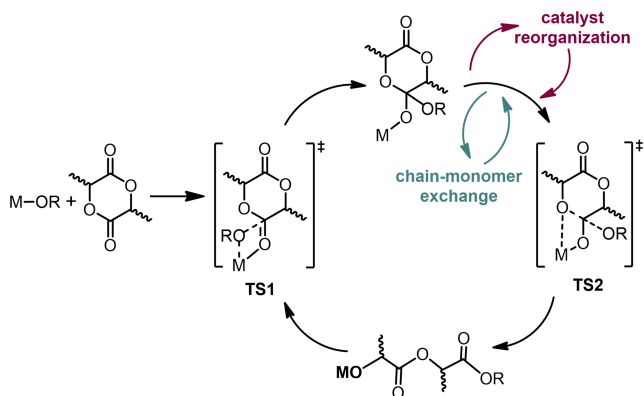


Fig. 2 Proposed coordination-insertion mechanism for stereoselective ROP of LA with the traditional pathway in black and additional pathways in burgundy and teal.

Previous studies have shown that the mechanism of stereocontrol may be influenced by the nature of the catalyst or the growing polymer chain.⁸ Isotactic or heterotactic PLA generally results from enantiomeric site control, in which the chirality of the catalyst controls the stereochemistry of the next monomer inserted into the growing polymer chain. On the other hand, control of the chirality of the incoming monomer unit by the last inserted lactidyl unit in the growing polymer chain produces heterotactic or syndiotactic PLA via a chain-end control mechanism.⁸ In a "dual-stereocontrol" mechanism, both the catalyst's chirality and the proximal stereogenic center of the last inserted lactidyl unit combine to define the stereochemistry of the growing polymer chain, leading to the formation of heterotactic or syndiotactic

PLA, respectively.

The dual-stereocontrol mechanism was recently cited to rationalize the level of stereocontrol observed in the stereoselective ROP of *rac*-LA and *meso*-LA using enantiopure chiral Al-alkoxide salan catalysts with bipyrrrolidine^{2,22} or binaphthyl^{19,20} backbones. Experiments involving the ROP of LA using an Al-alkoxide salan catalyst, (*R,R*)-LigAl-OBn, denoted (*R,R*)-1 in Figure 3, suggest that even though ring-opening of LA adjacent to the *R* stereocenter is kinetically favored, the alternative stereoisomer is thermodynamically favored. Specifically, when the reactions are performed under conditions to favor the thermodynamic product, ring opening occurs close to the *R* stereocenter of LA, but the initiation or polymerization product in which the *S* stereocenter of LA is proximal to Al is favored.^{2,23}

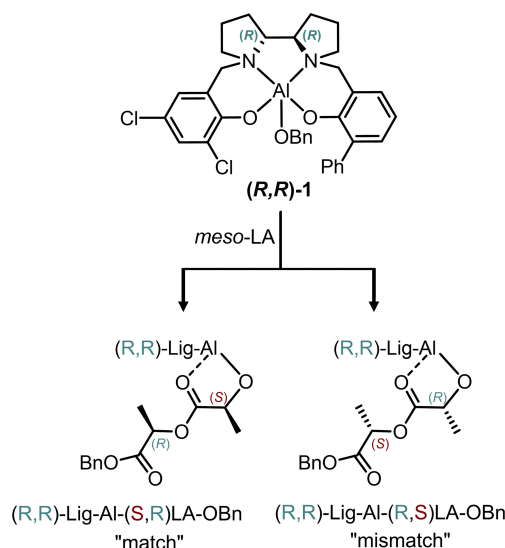


Fig. 3 "Match" (left) and "mismatch" (right) products formed from the stereoselective initiation ROP of *meso*-LA by the chiral Al-alkoxy catalyst, (*R,R*)-1.

Using a computational approach for catalytic design based on density functional theory (DFT), we seek to provide insight into the factors affecting the initiation step in the ROP of LA using (*R,R*)-1.^{23,24} A proposed ROP mechanism involving active site reorganization and changes in ligand wrapping along the reaction path is investigated to understand their impact on stereoselectivity.^{13,17} This understanding is a first step towards rational catalyst design for achieving precise control over stereochemistry in ROP reactions to obtain desired PLAs. This work focuses on the initiation step due to the aforementioned characterization of the first-insertion product using a benzyl initiator by Peterson *et al.*²³ Using DFT, the factors influencing chiral catalyst recognition in the ROP of *meso*-LA with (*R,R*)-1 were explored. These catalysts have a fixed chirality at the metal site, eliminating potential effects on polymer stereoregularity.¹⁴ Since *meso*-LA contains two different (*R* and *S*) stereogenic centers, it serves as an ideal substrate to study factors influencing stereocontrol in the synthesis of highly desired syndiotactic PLA.



2 Computational Details

To understand the initiation step in the stereoselective polymerization of *meso*-LA by (*R,R*)-**1**, we turned to Density Functional Theory (DFT) due to its efficiency in modeling catalytic reactions.^{24,25} All DFT computations were performed as implemented in the Gaussian 16 package.²⁶ However, these systems require careful conformational sampling and DFT is too computationally demanding for this portion of the work; therefore, tight-binding methods were also used. Specifically, conformational sampling was performed at the GFN2-xTB level using the Conformer-Rotamer Ensemble Sampling Tool (CREST) algorithm as implemented in the xTB package.^{27,28} The conformers generated by CREST were sorted using the Commandline Energetic Sorting (CENSO) algorithm.²⁹

DFT geometry optimizations were performed on the most stable conformers using the M06-L density functional³⁰ and the 6-31+G(d,p) basis set³¹. Harmonic vibrational analysis was employed to confirm the nature of all stationary points as minima or transition state structures.³² To verify that the single imaginary frequency is connected to the reactants and products for each transition state structure, intrinsic reaction coordinate (IRC) calculations were performed.³³ The free energies were corrected using the concentrations of 0.017M for catalysts and 1M for all reactants in order to represent the experimental conditions for the catalyst and standard state conditions for all other reactants and products.²³ Grimme's quasi-harmonic correction was applied to vibrational frequencies lower than 50 cm⁻¹. These corrections were used as implemented in the GoodVibes program.³⁴ Gibbs free energies were computed at 298.15 K. Single point calculations were carried out on all optimized geometries using the M06-2X functional³⁵ and the 6-311+G(d,p) basis set. To obtain total free energies of improved accuracy, thermal contributions to free energy from the M06-L/6-31+G(d,p) level of theory were added to the electronic energies from the single-point calculations. Solvation effects were included using the continuum solvation model based on density (SMD) for toluene in all calculations in order to model experimental conditions.^{23,36} The analysis of non-covalent interactions was carried out using the Multiwfn program package.³⁷

3 Results and Discussion

The initiation of *meso*-LA was modeled along multiple reaction pathways depending on the coordination mode of the catalyst and the prochiral face of the LA unit to which the alkoxy initiator is exposed. Momentarily setting aside the stereochemistry in the LA group itself, there are three coordination modes accessible for the monomer based on the respective orientation with the bipyrrrolidine ligand backbone and the alkoxy initiator (Figure 4a). One possibility is that the alkoxy group is oriented equatorial (*e*) to the bipyrrrolidine backbone of the catalyst. Equatorial orientation can yield two different wrapping modes of the oxygen-containing arms of the catalyst (denoted *e*₁ and *e*₂) along the reaction path. In *e*₁, the two oxygen centers (shown in black) coordinate to Al on the bipyrrrolidine ligand and are *cis* to one another, while in *e*₂ they are *trans* to one another. An alternative coordination mode

can be obtained when the alkoxy initiator is oriented axially (*a*) with respect to the catalyst backbone.

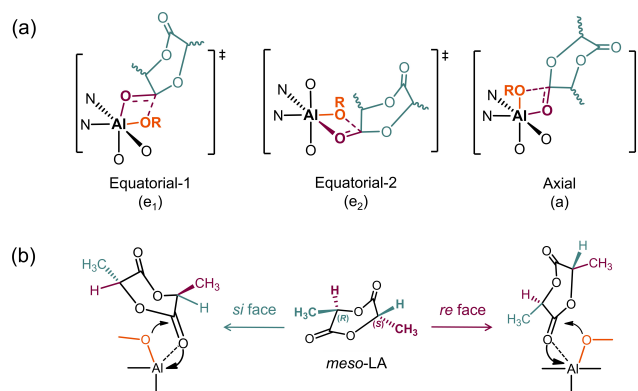


Fig. 4 Factors influencing the manner in which LA coordinates in the initiation step. (a) The three coordination modes (two equatorial and one axial) for the first transition state (TS1) with *meso*-LA. (b) The initial step for *meso*-LA can proceed via the *si* or *re* face. The alkoxy initiator is shown in orange, the LA monomer in green with its coordinating acyl unit in purple, and the coordinating atoms from the bipyrrrolidine ligand in black.

In order to understand the manner in which ring-opening occurs, several mechanisms are compared in which the initiator or the arms of the bipyrrrolidine ligand are rotated with respect to the incoming LA-monomer. The first assumption one could make is that coordination modes are unchanged throughout the coordination-insertion and ring-opening steps of ROP (Mechanism **M1**, Figure 5), leading to three pathways based on the coordination modes of the starting arrangements (**M1-A**, **M1-B**, and **M1-C**). Setting aside for now that each specific profile must correspond to an *R* or *S* stereocenter depending on the chirality of the stereocenter adjacent to the acyl unit coordinated to the Al center after ring-opening, the two prochiralities of the monomer are first considered, *si* or *re* (Figure 4b). For example, the **M1-A** pathway will be denoted **M1-A-re** or **M1-A-si** to distinguish the prochirality. This results in six pathways for each stereocenter: two prochiralities from each coordination mode: *e*₁, *e*₂, and *a*.

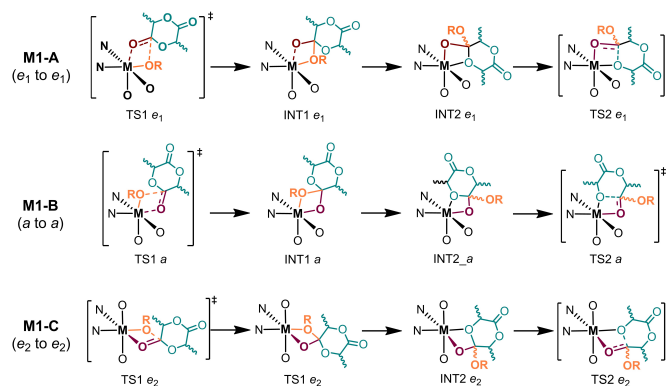


Fig. 5 A representation of mechanism 1 (**M1**) where the coordination modes are unchanged throughout the coordination-insertion and ring-opening steps of ROP. Pathways **M1-A**, **M1-B**, and **M1-C** begin from *e*₁, *e*₂, and *a* coordination modes, respectively.



An alternative could be that the wrapping of the arms on the bipyrrrolidine ligand remains preserved, but a rotation occurs during the reaction between the coordination sites of the LA-monomer and the alkoxy initiator. In Figure 4a, the two coordination modes with the same ligand wrapping are e_1 and a ; therefore, two options are available: 1) an exchange from e_1 to a , or 2) an exchange from a to e_1 (Mechanism **M2**, Figure 6). This leads to four possible mechanisms, since both prochiralities must be explored.

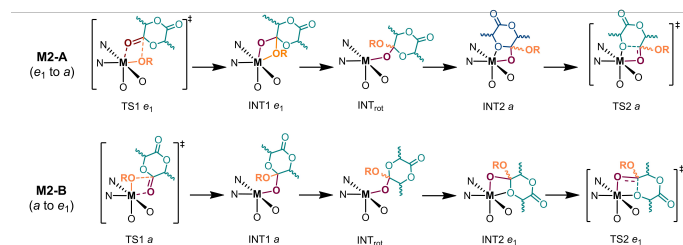


Fig. 6 A representation of mechanism 2 (**M2**) where the wrapping of the arms on the bipyrrrolidine ligand remains unchanged, but a rotation between the coordination sites of the LA-monomer and the alkoxy initiator occurs during the reaction. Pathways M2-A and M2-B begin from the e_1 and a coordination modes. This mechanism is not accessible beginning with the e_2 coordination mode.

The final set of mechanisms involve changes in the wrapping mode of the bipyrrrolidine ligand, which occurs between the nucleophilic attack (**TS1**) and ring-opening (**TS2**) steps of ROP (Mechanism 3 (**M3**), Figure 7). This leads to four possible changes with respect to coordination mode: 1) from e_1 to e_2 in **M3-A**, 2) from a to e_2 in **M3-B**, 3) from e_2 to e_1 in **M3-C**, and 4) from e_2 to a in **M3-D**. Once more, both prochiralities are considered resulting in a total of eight pathways.

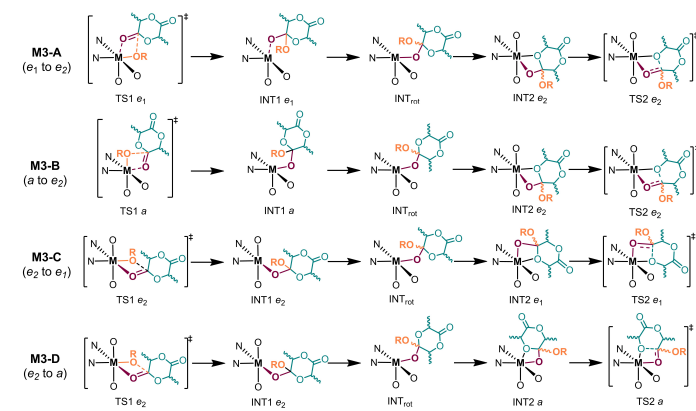


Fig. 7 A representation of mechanism 3 (**M3**), which involves changes in the wrapping mode of the bipyrrrolidine ligand. Pathways A, B, C, and D begin from the three coordination modes, with two options accessible beginning with e_2 .

Given the number of profiles to be considered, the discussion will walk through the three categories of mechanisms in order. This will include mechanisms where ring opening preferentially occurs close to the R stereocenter of LA in *meso*-LA, resulting in

the S stereocenter being proximal to the metal after ring opening. These reactions will be referred to as “*meso*-S-LA” for clarity. Likewise, the discussion of the analogous pathways when ring opening occurs adjacent to the S stereocenter in *meso*-LA, resulting in the R stereocenter being closer to the metal after ring opening (referred to as “*meso*-R-LA”), will also be presented.

Recall that the first set of proposed mechanisms, **M1**, does not involve a change in ligand wrapping throughout the reaction profile (Figure 5). The first step, **TS1**, is the barrier involving the attack of the initiator. Note that the other mechanisms, **M2** and **M3**, also start with the same first step since initiation occurs independently of how the wrapping mode evolves throughout the subsequent reaction. In *meso*-S-LA (Table 1), a clear preference for the e_1 coordination mode is shown resulting in a barrier of 12.7 kcal/mol with either prochirality. On the other hand, when the a coordination mode is computed, the barrier increases to 18.4 and 27.8 kcal/mol for *re* and *si*, respectively. The e_2 coordination mode results in energies lower than a but higher than e_1 with values of 13.4 and 16.1 kcal/mol for *re* and *si*, respectively. We note in passing that these energies were obtained following conformational searches which were essential for these species since energies were lowered by as much as 6 kcal/mol for some transition state structures (Figure S1).

A closer look at the **TS1** geometries of the e_1 coordination mode show key ligand-chain non-covalent interactions (NCIs) between the benzyloxy initiator and monomer unit/phenoxy ligands, including hydrogen bonding ($O\cdots H$ lengths range from 2.45 to 2.63 Å). Similar interactions are also observed between the monomer unit and the catalyst backbone. These NCIs induce stabilizing effects, resulting in the relatively lower energy barriers observed (Figures 8 and S2, left). On the other hand, in the respective geometries for the a and e_2 coordination modes, the stabilizing non-covalent interactions are less pronounced (Figures 8 and S2).

Table 1 Pathways for the stereoselective initiation of *meso*-S-LA by LigA-IObn. All free energies (kcal/mol) are computed taking the free catalyst and monomer lactide as the reference, except the relative reaction barriers for **TS2** (in parenthesis), which are computed relative to the most stable intermediate in the pathway.

Path	TS1	INT1	INT _{rot}	INT2	TS2
M1-A- <i>re</i>	12.7	8.0	–	7.3	13.8 (6.5)
M1-A- <i>si</i>	12.7	7.3	–	7.3	16.7 (9.4)
M1-B- <i>re</i>	18.4	11.2	–	8.4	20.8 (12.4)
M1-B- <i>si</i>	27.8	14.0	–	5.6	24.4 (18.8)
M1-C- <i>re</i>	13.4	10.8	–	19.8	21.8 (2.0)
M1-C- <i>si</i>	16.1	11.3	–	9.6	15.1 (5.5)
M2-A- <i>re</i>	12.7	8.0	4.3	8.4	20.8 (16.5)
M2-A- <i>si</i>	12.7	7.3	6.3	5.6	24.4 (18.8)
M2-B- <i>re</i>	18.4	11.2	4.3	7.3	13.8 (9.5)
M2-B- <i>si</i>	27.8	14.0	6.3	7.3	16.7 (10.4)
M3-A- <i>re</i>	12.7	8.0	4.3	19.8	21.8 (17.5)
M3-A- <i>si</i>	12.7	7.3	6.3	9.6	15.1 (8.8)
M3-B- <i>re</i>	18.4	11.2	4.3	19.8	21.8 (17.5)
M3-B- <i>si</i>	27.8	14.0	6.3	9.6	15.1 (8.8)
M3-C- <i>re</i>	13.4	10.8	4.3	7.3	13.8 (9.5)
M3-C- <i>si</i>	16.1	11.3	6.3	7.3	16.7 (10.4)
M3-D- <i>re</i>	13.4	10.8	4.3	8.4	20.8 (16.5)
M3-D- <i>si</i>	16.1	11.3	6.3	5.6	24.4 (18.8)



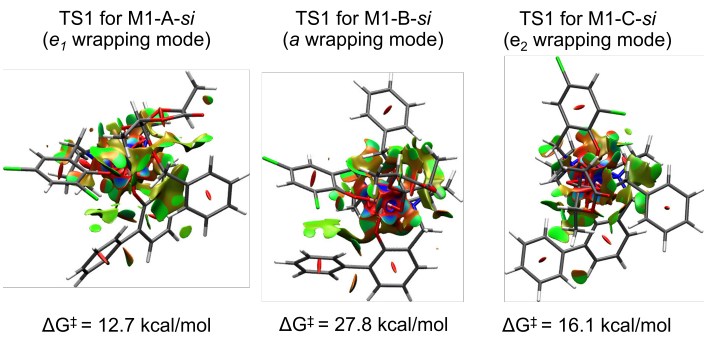


Fig. 8 TS1 structures showing selected non-covalent interactions (NCIs) for *meso*-S-LA. Significant non-covalent interactions (NCIs) between the benzyloxy initiator and monomer unit/ phenoxy ligands, and between the monomer unit and the catalyst backbone contribute to the stabilization of TS1 geometry from M1-A-*si* (*e*₁, left, 12.7 kcal/mol), compared to the corresponding geometry from M1-B-*si* (*a*, middle, 27.8 kcal/mol) per the distribution of the green contours representing van der Waal's interactions. M1-C-*si* (*e*₂, right, 16.1 kcal/mol) showed intermediate stability. Blue contours represent strong attraction, including hydrogen/ halogen bonds while the red contour represents strong repulsion, including steric effects in the ring and cage. Note that the labels for TS1 are for M1; however, these initiation structures are included in M2 and M3 profiles as well.

Additionally, the initiation step in *meso*-R-LA is explored (Table 2). If the *e*₁ coordination mode is used (M1-A), the barriers are 14.8 and 9.4 kcal/mol for *re* and *si*, respectively. Compared to *meso*-S-LA, the barrier for initiation (TS1) is higher in the *re* prochirality but lower for the *si* prochirality. As was the case for *meso*-S-LA, the barriers for the mechanism for *meso*-R-LA with the *a* coordination mode (M1-B) are the highest, with values of 22.1 and 31.3 kcal/mol for the *re* and *si* prochiralities, respectively. Finally, the barriers for the initiation step with the *e*₂ coordination mode (M1-C) are higher compared to the corresponding values with *meso*-S-LA, for both *re* at 14.4 kcal/mol and *si* at 29.3 kcal/mol. Overall, the lowest barriers to initiation for either *meso*-S-LA or *meso*-R-LA have the wrapping mode *e*₁. Specifically, the profile labeled M1-A-*si* with *meso*-R-LA had the lowest TS1 barrier. As was previously noted for *meso*-S-LA, the stability of the TS1 geometries in *e*₁ can be attributed to important interactions between the monomer, benzyloxy chain, and ligands including the bipyrrrolidine group in the polymer backbone and the Cl-substituted phenoxy group. Changes in the coordination mode of the LA unit and alkoxy initiator in *a* and changes in the wrapping mode of the ligand in *e*₂ result in monomer orientations that eliminate many of these stabilizing interactions in the transition state structure, leading to higher energy barriers (Figure S3).

The next step involves the formation of an intermediate in which the alkoxy initiator, in this case the benzyloxy group, is coordinated to the carbonyl carbon on the lactone. The variations among the profiles (M1, M2, and M3) stem from the differences in wrapping mode that occur in the steps after INT1. First, continuing along the M1 mechanism where the coordination mode remains constant throughout the reaction profile, we begin by discussing *meso*-R-LA. INT1 results from insertion of LA between the catalyst and the alkoxy group in the initiation step, resulting in the coordination of the monomer to Al via an acyl oxygen.

Table 2 Pathways for the stereoselective initiation of *meso*-R-LA by LigA-IOBn. All free energies (kcal/mol) are computed taking the free catalyst and monomer lactide as the reference, except the relative reaction barriers for TS2 (in parenthesis), which are computed relative to the most stable intermediate in the pathway.

Path	TS1	INT1	INT _{rot}	INT2	TS2
M1-A- <i>re</i>	14.8	10.1	–	8.8	13.2 (4.4)
M1-A- <i>si</i>	9.4	8.8	–	11.2	18.2 (7.0)
M1-B- <i>re</i>	22.1	7.2	–	9.7	13.9 (4.2)
M1-B- <i>si</i>	31.3	8.9	–	11.5	23.5 (12.0)
M1-C- <i>re</i>	14.4	10.9	–	9.2	14.8 (5.6)
M1-C- <i>si</i>	29.3	14.3	–	16.0	16.7 (0.7)
M2-A- <i>re</i>	14.8	10.1	3.2	9.7	13.9 (10.7)
M2-A- <i>si</i>	9.4	8.8	8.0	11.5	23.5 (15.5)
M2-B- <i>re</i>	22.1	7.2	3.2	8.8	13.2 (10.0)
M2-B- <i>si</i>	31.3	8.9	8.0	11.2	18.2 (10.2)
M3-A- <i>re</i>	14.8	10.1	3.2	9.2	14.8 (11.6)
M3-A- <i>si</i>	9.4	8.8	8.0	16.0	16.7 (8.7)
M3-B- <i>re</i>	22.1	7.2	3.2	9.2	14.8 (11.6)
M3-B- <i>si</i>	31.3	8.9	8.0	16.0	16.7 (8.7)
M3-C- <i>re</i>	14.4	10.9	3.2	8.8	13.2 (10.0)
M3-C- <i>si</i>	29.3	14.3	8.0	11.2	18.2 (10.2)
M3-D- <i>re</i>	14.4	10.9	3.2	9.7	13.9 (10.7)
M3-D- <i>si</i>	29.3	14.3	8.0	11.5	23.5 (15.5)

However, a second oxygen on the lactone ring must coordinate in order to be properly aligned for ring-opening. The intermediate that reflects this reorganization prior to ring-opening is denoted INT2. Following INT2, the transition state for ring-opening (TS2) is reported (Table 2). While a clear trend does not emerge for TS1, in TS2 the barriers are lower for the *re* prochirality. Comparing the six possibilities for the M1 profile with *meso*-R-LA, the one with the lowest barriers, 14.8 and 13.2 kcal/mol for TS1 and TS2, respectively, is denoted M1-A-*re*. Turning to *meso*-S-LA for comparison, a profile with slightly lower barriers is obtained for the so-called M1-A-*re* pathway (barriers of 12.7 for TS1 and 13.8 kcal/mol for TS2). It is worth noting that in the TS2 geometry for *e*₁, the highest barrier in the most favorable pathway (M1-A-*re* for *meso*-S-LA), coordination of the benzyloxy group to the *re* surface permits additional stabilizing NCIs between the benzyl chain and the backbone bipyrrrolidine group (Figure S4, left). This is in addition to the NCIs previously mentioned between the monomer and phenoxy ligands of (R,R)-1, which are significantly facilitated by the *S* configuration of the monomer adjacent to the Al center. Similar stabilizing NCIs are present in the TS2 geometry of the corresponding M1-A-*re* pathway for *meso*-R-LA (Figure S4, middle). However, in the high-energy TS1 geometry for this *e*₁ coordination mode, such stabilizing interactions between the polymer chain and phenoxy ligands are counteracted by repulsion between methyl groups at the *S* stereocenter of the monomer and the backbone bipyrrrolidine group (Figure S4, right).

On the other hand, the second set of mechanisms considered (M2) examines whether the barriers would be reduced if the wrapping of the arms on the bipyrrrolidine ligand is preserved, while a rotation between the coordination sites of the LA-monomer and the alkoxy initiator is permitted following INT1 (Figure 6). In all of the cases with both *meso*-S-LA and *meso*-R-LA, the barriers are higher than those obtained for M1-A-*re* (Figure 9). However, the lowest barriers obtained for *meso*-S-LA were



for the profile denoted **M2-B-re**, which involves a change of coordination mode from axial (*a*) to equatorial (*e*₁) as it proceeds from **INT1** to **INT2** via **INT_{rot}**. Note that attempts to converge a transition state associated with this rotation were unsuccessful, though we expect it to be lower than the barriers associated with the bond-making and breaking-steps in **TS1** and **TS2**. Since the **M2** profiles are higher energy than the **M1** pathways, these TS structures were not pursued further. Nevertheless, the lowest barriers for *meso*-R-LA were obtained for **M2-A-re**. Here, the coordination mode changes from equatorial to axial as one proceeds from **INT1** to **INT2** via **INT_{rot}**. Considering the geometries of the rate-determining transition states (RDTs), as defined by Kozuch and Martin,³⁸ the equatorial orientation of **TS1** in the **M2-A-re** pathway of *meso*-R-LA is observed to prime the structure for the formation of favorable NCIs between the benzyl chain and the Cl-substituted phenoxy ligand. However, this important interaction is missing in the **TS1** geometry of the **M2-B-re** pathway for *meso*-S-LA due to the axial orientation, accounting for the resulting high free energy barrier, in spite of other NCIs being present (Figure S5). For *meso*-S-LA, the presence of favorable NCIs account for the stability of the **M1** pathway compared to the **M2** pathway. However, no distinction can be made between the **M1** and **M2** pathways for *meso*-R-LA with respect to the RDTs (Table 1 and Table 2).

The final class of mechanisms considered, and the one involving the most rearrangements in the ligands and coordination modes, is denoted **M3** (Figure 7). Unlike the **M1** and **M2** pathways, the **M3** profiles involve changes in the wrapping mode of the bipyrrrolidine ligand following **INT1**. The reactions proceed first through a rotation (**INT_{rot}**) followed by the barrier to the rotation (**TS_{rot}**), until the final intermediate (**INT2**) and ring-opening transition state (**TS2**) are obtained. Once again, the majority of the orientations considered result in higher barriers compared to **M1-A-re**; however, the **TS2** barrier in **M3-C-re** for *meso*-S-LA remains the same at 13.8 kcal/mol while the **TS1** barrier is slightly higher at 13.4 kcal/mol compared to the **TS1** barrier of 12.7 kcal/mol in the **M1-A-re** pathway. For the **M3** mechanisms with *meso*-R-LA, the lowest barriers were obtained for **M3-C-re** and **M3-D-re**; however, both are higher than the *meso*-S-LA **M3-C-re** profile and as a result are not discussed in detail.

The lowest energy profiles have been summarized in Figure 9 to make comparisons between *meso*-S-LA and *meso*-R-LA. Recall that the results are only sorted as “*meso*-S-LA” and “*meso*-R-LA” for organization purposes since both stereocenters are present in *meso*-LA and either could be proximal to the Al center upon initiation. The profile with the lowest energy RDTs for *meso*-S-LA was **M1-A-re** while that of *meso*-R-LA was **M3-C-re**. This implies that for *meso*-R-LA and *meso*-S-LA, the most favorable energy profiles are obtained through different coordination modes for the monomer via changes in ligand wrapping. The geometry that manifests for the active site of the catalyst (*R,R*)-**1** depends on the relative chirality of the way in which the monomer coordinates during stereo-controlled ring opening polymerization.

Overall, these results demonstrate that ring opening *meso*-LA at the C–O bond proximal to the *R* stereocenter to form the “match” product is kinetically favored over ring-opening at the *S* stere-

ocenter to form the “mismatch” product by 0.6 kcal/mol. This is based on the RDTs from the most favorable pathways summarized in Figure 9 and consistent with experimental observations.^{2,14,23} Specifically, the RDTs for *meso*-S-LA is 13.8 kcal/mol in the **M1-A-re** pathway, while for *meso*-R-LA the RDTs is 14.4 kcal/mol in the **M3-C-re** pathway ($\Delta\Delta G^\ddagger = 0.6$ kcal/mol). For *meso*-S-LA, the lower barriers for initiation are critical to achieving the stereoselective behavior observed with (*R,R*)-**1**, since the barriers associated with ring-opening (**TS2**) become the RDTs. On the other hand, the higher initiation barriers for *meso*-R-LA mean that **TS1** is the RDTs for these pathways. These results are consistent with the polymer products produced when experiments are performed under kinetically driven conditions.^{2,14,23} Similar stereoselectivities have also been reported in the ROP of *meso*-LA by the Spassky catalyst.¹³

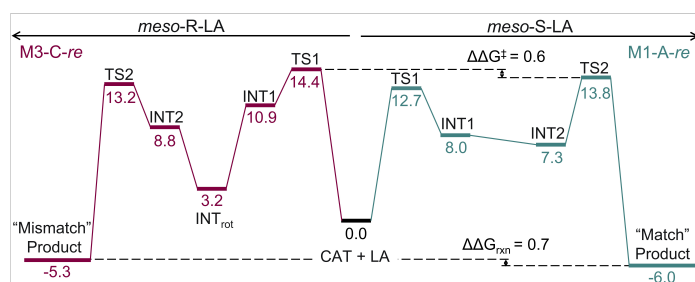


Fig. 9 Minimum energy profiles for *meso*-R-LA and *meso*-S-LA. Specifically, the **M3-C-re** (burgundy) and the **M1-A-re** (teal) and mechanisms are shown in kcal/mol. $\Delta\Delta G^\ddagger$ and $\Delta\Delta G_{\text{rxn}}$ are indicated with dashed lines.

Additionally, the resulting initiation product for *meso*-S-LA is more thermodynamically stable with respect to reactants ($\Delta G_{\text{rxn}} = -6.0$ kcal/mol) than the corresponding product for *meso*-R-LA ($\Delta G_{\text{rxn}} = -5.3$ kcal/mol) (Figure 10). In the former, the *S* stereocenter of the lactidyl unit is proximal to the metal after ring opening. This was first referred to as the “match” complex by Hador *et al.*² and is the major product in the first-insertion step of the stereocontrolled ROP of both *rac*-LA and *meso*-LA by (*R,R*)-**1**.^{2,23} On the other hand, formation of the initiation product where the *R* stereocenter of the lactidyl unit is proximal to the metal center after ring-opening yields was referred to as the “mismatch” product. The small energy difference between the first-insertion products obtained by DFT ($\Delta\Delta G_{\text{rxn}} = 0.7$ kcal/mol) is consistent with the experimentally observed match:mismatch ratio of 67:33.²³

As was the case in the transition states, a close examination of the initiation product geometries reveals the importance of ligand-chain NCIs in stabilizing the products with different stereoisomers. NCIs between the Cl-substituted phenoxy ligand and the polymer chain appear to exert greater stabilizing effects in the “match” product compared to similar interactions between the former and the bipyrrrolidine group of the catalyst backbone in the “mismatch” product. Additional NCIs between the phenoxy ligands and the catalyst backbone provide further stabilizing effects in both products (Figures 10 and S6). These subtle differences in interactions result from the orientations of the polymer chain due to rotations about the *S* or *R* stereocenters and drive

the formation of the "match" product. Therefore, DFT shows that the stereoselective ROP of *meso*-LA involves both a kinetic and thermodynamic preference for the "match" product. Our results are consistent with the observation of the "match" as the major product for experiments examining initiation products for *meso*-LA, using (*R,R*)-**1**, under experimental conditions favoring thermodynamic control.^{2,23}

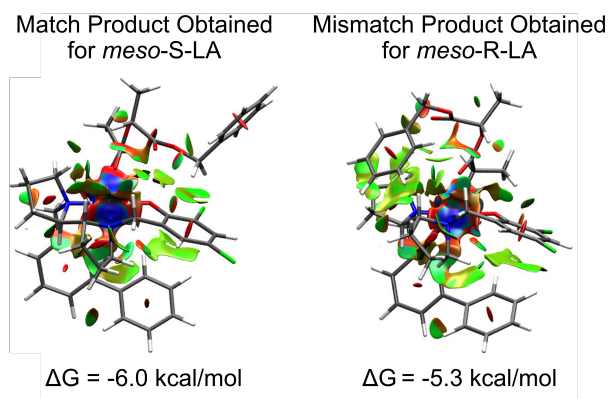


Fig. 10 DFT-optimized geometries of the "match" and "mismatch" initiation products of *meso*-LA and the (*R,R*)-LigAlOBn catalyst showing ligand-chain non-covalent interactions. Black ring around methylene group highlights orientation of the interacting polymer chain due to rotations about the *S* or *R* stereocenters. Blue contours represent strong attraction, including hydrogen/halogen bonds while the red contour represents strong repulsion, including steric effects in the ring and cage. Al in pink, C in gray, Cl in green, N in blue, O in red, H in white.

4 Conclusions

The chloride-substituted, bipyrrrolidine-based Al-alkoxy salan catalyst shows kinetic preference for the stereoselective ring-opening of *meso*-LA at the carbonyl unit adjacent to the *R* stereocenter, leading to a thermodynamic preference for the resulting initiation product in which the *S* stereocenter is adjacent to Al after ring opening to yield what has been previously referred to as the "match" product. During the initiation steps, both the rate-determining transition states and products correspond to the "match" complex, which are stabilized by non-covalent interactions (NCIs). This also presents challenges for computational modeling of such catalysts, especially as one considers moving to study propagation steps which are crucial in the proposed dual-stereocontrol mechanism. Conformational sampling must be performed in both the intermediates and transition state structures to identify structures within a kcal/mol. Even when doing so, care must be taken to ensure that NCIs that could further stabilize important intermediate or TS are not neglected as this can impact one's ability to predict selectivities accurately. While in solution, a variety of conformers will be present, each DFT mechanism represents a static picture. Nevertheless, DFT can provide insight into the nature of the NCIs one should consider and show how changing which stereocenter is proximal to the metal impacts these interactions in a meaningful way.

5 Author Contributions

SAF performed the DFT calculations and wrote the first draft. BV supervised the project and acquired funding. All authors analyzed the data and the final manuscript was written with the contribution of all authors.

6 Data Availability

Data for this article, including XYZ coordinates and output files are available in a FigShare repository (<https://doi.org/10.6084/m9.figshare.29852522>).

7 Acknowledgements

The authors thank Appie Peterson and Bill Tolman for fruitful discussions. This work was supported by the National Science Foundation (NSF) Center for Sustainable Polymers under Award Number CHE-1901635. Computations supporting this project were performed on the High Performance Computing systems at the University of South Dakota, funded by NSF Award OAC-1626516.

Notes and references

- 1 J. M. Becker and A. P. Dove, in *Poly(lactide)s as Robust Renewable Materials*, John Wiley & Sons, Ltd, 2011, ch. 9, pp. 201–220.
- 2 R. Hador, A. Botta, V. Venditto, S. Lipstman, I. Goldberg and M. Kol, *Angew. Chem. Int. Ed.*, 2019, **58**, 14679–14685.
- 3 S. Bian, S. Abbina, Z. Lu, E. Kolodka and G. Du, *Organometallics*, 2014, **33**, 2489–2495.
- 4 F. M. Haque, J. S. A. Ishibashi, C. A. L. Lidston, H. Shao, F. S. Bates, A. B. Chang, G. W. Coates, C. J. Cramer, P. J. Dauenhauer, W. R. Dichtel, C. J. Ellison, E. A. Gormong, L. S. Hamachi, T. R. Hoye, M. Jin, J. A. Kalow, H. J. Kim, G. Kumar, C. J. LaSalle, S. Liffland, B. M. Lipinski, Y. Pang, R. Parveen, X. Peng, Y. Popowski, E. A. Prebhalo, Y. Reddi, T. M. Reineke, D. T. Sheppard, J. L. Swartz, W. B. Tolman, B. Vlaisavljevich, J. Wissinger, S. Xu and M. A. Hillmyer, *Chem. Rev.*, 2022, **122**, 6322–6373.
- 5 V. Sangeetha, H. Deka, T. Varghese and S. Nayak, *Polymer Composites*, 2018, **39**, 81–101.
- 6 G. Li, M. Zhao, F. Xu, B. Yang, X. Li, X. Meng, L. Teng, F. Sun and Y. Li, *Molecules*, 2020, **25**, 5023.
- 7 E. Balla, V. Daniilidis, G. Karlioti, T. Kalamas, M. Stefanidou, N. D. Bikiaris, A. Vlachopoulos, I. Koumentakou and D. N. Bikiaris, *Polymers*, 2021, **13**, 1822.
- 8 M. J. Stanford and A. P. Dove, *Chem. Soc. Rev.*, 2010, **39**, 486–494.
- 9 R. T. Mathers and M. A. Meier, *Green polymerization methods: renewable starting materials, catalysis and waste reduction*, John Wiley & Sons, 2011.
- 10 C. M. Thomas, *Chem. Soc. Rev.*, 2010, **39**, 165–173.
- 11 P. J. Dijkstra, H. Du and J. Feijen, *Polym. Chem.*, 2011, **2**, 520–527.
- 12 M. J.-L. Tschan, R. M. Gauvin and C. M. Thomas, *Chem. Soc. Rev.*, 2021, **50**, 13587–13608.



- 13 M. C. D'Alterio, C. De Rosa and G. Talarico, *Chem. Commun.*, 2021, **57**, 1611–1614.
- 14 R. Hador, S. Lipstman, R. Rescigno, V. Venditto and M. Kol, *Chem. Commun.*, 2020, **56**, 13528–13531.
- 15 N. G. Khouri, J. O. Bahú, C. Blanco-Llamero, P. Severino, V. O. Concha and E. B. Souto, *J. Mol. Struct.*, 2024, **1309**, 138243.
- 16 O. Dechy-Cabaret, B. Martin-Vaca and D. Bourissou, *Chem. Rev.*, 2004, **104**, 6147–6176.
- 17 M. C. D'Alterio, C. De Rosa and G. Talarico, *ACS Catal.*, 2020, **10**, 2221–2225.
- 18 N. Spassky, M. Wisniewski, C. Pluta and A. L. Borgne, *Macromol. Chem. Phys.*, 1996, 2627–2637.
- 19 T. M. Ovitt and G. W. Coates, *J. Am. Chem. Soc.*, 1999, **121**, 4072–4073.
- 20 T. M. Ovitt and G. W. Coates, *J. Am. Chem. Soc.*, 2002, **124**, 1316–1326.
- 21 T. M. Ovitt and G. W. Coates, *J. Am. Chem. Soc.*, 1999, **124**, 1316–1326.
- 22 K. Press, I. Goldberg and M. Kol, *Angew. Chem. Int. Ed.*, 2015, **54**, 14858–14861.
- 23 A. Peterson, R. Hador, M. Pink, Y. Popowski, M. Kol and W. B. Tolman, *J. Am. Chem. Soc.*, 2022, **144**, 20047–20055.
- 24 J. G. Vitillo, C. J. Cramer and L. Gagliardi, *Isr. J. Chem.*, 2022, **62**, e202100136.
- 25 M. Bursch, J.-M. Mewes, A. Hansen and S. Grimme, *Angew. Chem. Int. Ed.*, 2022, **61**, e202205735.
- 26 M. J. Frisch, G. W. Trucks, H. B. Schlegel, G. E. Scuseria, M. A. Robb, J. R. Cheeseman, G. Scalmani, V. Barone, G. A. Petersson, H. Nakatsuji, X. Li, M. Caricato, A. V. Marenich, J. Bloino, B. G. Janesko, R. Gomperts, B. Mennucci, H. P. Hratchian, J. V. Ortiz, A. F. Izmaylov, J. L. Sonnenberg, D. Williams-Young, F. Ding, F. Lipparini, F. Egidi, J. Goings, B. Peng, A. Petrone, T. Henderson, D. Ranasinghe, V. G. Zakrzewski, J. Gao, N. Rega, G. Zheng, W. Liang, M. Hada, M. Ehara, K. Toyota, R. Fukuda, J. Hasegawa, M. Ishida, T. Nakajima, Y. Honda, O. Kitao, H. Nakai, T. Vreven, K. Throssell, J. A. Montgomery, Jr., J. E. Peralta, F. Ogliaro, M. J. Bearpark, J. J. Heyd, E. N. Brothers, K. N. Kudin, V. N. Staroverov, T. A. Keith, R. Kobayashi, J. Normand, K. Raghavachari, A. P. Rendell, J. C. Burant, S. S. Iyengar, J. Tomasi, M. Cossi, J. M. Millam, M. Klene, C. Adamo, R. Cammi, J. W. Ochterski, R. L. Martin, K. Morokuma, O. Farkas, J. B. Foresman and D. J. Fox, *Gaussian~16 Revision C.01*, 2016, Gaussian Inc. Wallingford CT.
- 27 S. Grimme, *J. Chem. Theory Comput.*, 2019, **15**, 2847–2862.
- 28 P. Pracht, F. Bohle and S. Grimme, *Phys. Chem. Chem. Phys.*, 2020, **22**, 7169–7192.
- 29 S. Grimme, F. Bohle, A. Hansen, P. Pracht, S. Spicher and M. Stahn, *J. Phys. Chem. A*, 2021, **125**, 4039–4054.
- 30 Y. Zhao and D. G. Truhlar, *J. Chem. Phys.*, 2006, **125**, 194101.
- 31 W. Hehre and L. Radom, *P. v R. Schleyer and JA Pople, Ab initio Molecular Orbital Theory*, 1986.
- 32 R. F. Ribeiro, A. V. Marenich, C. J. Cramer and D. G. Truhlar, *J. Phys. Chem. B*, 2011, **115**, 14556–14562.
- 33 F. Weigend and R. Ahlrichs, *Phys. Chem. Chem. Phys.*, 2005, **7**, 3297.
- 34 Y.-P. Li, J. Gomes, S. Mallikarjun Sharada, A. T. Bell and M. Head-Gordon, *J. Phys. Chem. C*, 2015, **119**, 1840–1850.
- 35 Y. Zhao and D. G. Truhlar, *Theo. Chem. Acc.*, 2008, **120**, 215–241.
- 36 A. V. Marenich, C. J. Cramer and D. G. Truhlar, *J. Phys. Chem. B*, 2009, **113**, 6378–6396.
- 37 T. Lu and F. Chen, *J. Comput. Chem.*, 2012, **33**, 580–592.
- 38 S. Kozuch and J. M. L. Martin, *ChemPhysChem*, 2011, **12**, 1413–1418.



Data Availability Statement

Data for this article, including XYZ coordinates and output files, are available in a FigShare repository at <https://doi.org/10.6084/m9.figshare.29852522>.

Open Access Article. Published on 04 September 2025. Downloaded on 9/23/2025 11:00:31 PM.
This article is licensed under a Creative Commons Attribution-NonCommercial 3.0 Unported Licence.

